Environmental Science: Atmospheres

ROYAL SOCIETY OF CHEMISTRY

PAPER

View Article Online
View Journal | View Issue

Cite this: *Environ. Sci.: Atmos.*, 2025, **5**, 1099

Multiphase reaction of nitrate radicals with vanillic acid aerosols: kinetics and formation of light-absorbing particles

Laura-Helena Rivellini, *[ab] Carolyn Liu-Kang [b] and Jonathan P. D. Abbatt *[b]

Given that biomass-burning aerosol emissions have a direct radiative effect on the atmosphere, it is important to understand the chemistry that occurs within wildfire smoke that may change aerosol particle optical properties. To investigate night-time aging chemistry, this laboratory study explores the kinetics of the reaction between gas-phase nitrate radicals (NO_3) and vanillic acid (VA), a functionalized phenol. As breakdown products of lignin, phenolic compounds are the commonly observed components of biomass burning smoke. They are also present in urban air pollution, formed by the oxidation of aromatic precursors. The study was conducted in an aerosol flow tube with a residence time of 15 minutes, where roughly 1.6 pptv of NO_3 was formed by the reaction of NO_2 (21 ppbv) and O_3 (230 ppbv), and VA/ammonium sulfate (AS) solutions were atomized to form particles in the accumulation mode size range. The reaction was monitored by an aerosol mass spectrometer (AMS), which measured nitrated aerosol products, and by a 5-wavelength aethalometer, which observed the optical absorption of aerosol particles. The observed gas-surface kinetics are consistent with a NO_3 reactive uptake coefficient to form a nitrated product of 0.30 ± 0.39 and 0.19 ± 0.12 at respectively RH $= 25\% \pm 5\%$ and $55\% \pm 5\%$ at 296 K. The aerosol particles became highly absorbing during the reaction in the near ultraviolet (375 nm) and visible (470, 528, and 625 nm) regions. While this change in absorptivity presumably arises *via* the nitration of the aromatic ring, the reaction drives stronger particle absorption, which extends much more deeply into the visible part of the spectrum than is characteristic of (mono) nitrovanillic acid (NVA), indicative of the formation of complex reaction products. These results demonstrate that night-time atmospheric aging of phenol-containing wildfire smoke and urban particulates will occur rapidly and significantly darken the particles throughout the visible part of the spectrum.

Received 8th June 2025
Accepted 7th August 2025

DOI: 10.1039/d5ea00066a

rsc.li/esatmospheres

Environmental significance

The chemical aging of biomass burning aerosols is important for climate. However, most studies have focused on daytime processes involving light, ozone, or hydroxyl radicals. Herein, we studied a key nighttime chemical process, the reaction of nitrate radicals (NO_3) with vanillic acid, a biomass burning particle surrogate. Using environmentally relevant NO_3 mixing ratios, we found that the kinetics are extremely rapid (on the timescale of minutes), with about 30% of NO_3 collisions with the particles forming nitrated products. For the first time, we document the changes in aerosol light absorption as a result of the reaction. The particles became substantially darker, with the increased absorption extending across all visible wavelengths. This is indicative of complex chemical aging processes.

1. Introduction

Biomass burning aerosol particles contain a diverse array of organic molecules, some arising from primary particulate emissions of the burning material and others *via* gas-to-particle partitioning and secondary processes. Many of these molecules have their origins in the cellulosic component of plant material leading to, for example, small sugars. Similarly, the lignin component of biofuel is transformed into smaller molecules during burning, including to a large number of functionalized phenols.[1,2] The presence of this complex molecular mixture in the atmosphere has impacts on both health and climate. In addition, phenols are formed within urban environments *via* the oxidation of aromatic precursors.[3,4] In particular, aerosol molecules that absorb actinic radiation in the visible and ultraviolet parts of the spectrum are referred to as brown carbon (BrC) materials.[5,6] The contribution of BrC to the direct radiative

[a]*NUS Environmental Research Institute, National University of Singapore, 117411, Singapore. E-mail: laura.rivellini21@gmail.com*
[b]*Department of Chemistry, University of Toronto, Toronto, M5S 3H6, ON, Canada. E-mail: Jonathan.abbatt@utoronto.ca*

effect is thought to be 25% of the radiative impact of black carbon particles.[7–9] This impact can be proportionally higher in regions of high wildfire impact, especially under smoldering fire conditions that produce a lot of particulate materials. Moreover, BrC is present in urban areas.[10–12]

As light-absorbing molecules, BrC aerosol materials are commonly electron-rich with a considerable degree of chemical unsaturation. These features make them prone to oxidative chemical transformations in the atmosphere. Field measurements on the rate at which BrC particles age in the atmosphere are challenging to conduct because the age of the fire or pollution plume needs to be known; nevertheless, there is an emerging consensus that aging affects the radiative impacts of BrC. In particular, significant whitening has been reported to occur far downwind of fire emissions, on a timescale as short as 24 hours.[13–16] Close to the fire source in the near-field, there is considerable variability in how BrC ages, with little indication of net whitening.[17] This could be because different darkening and whitening processes occur simultaneously.[18] The characteristics of the particles close to a fire are complex, with particle dilution and associated evaporation occurring simultaneously with secondary organic aerosol formation and multiphase chemical processing.[19]

Many laboratory studies have addressed the atmospheric chemical aging processes involving BrC aerosol particles,[5,6,18] including chemical transformations that occur in daylight hours *via* exposure to light and OH radicals.[18,20–31] These studies have illustrated that some wildfire materials initially become more absorptive in the near ultraviolet (UV) and visible parts of the spectrum, either *via* functionalization of reactive precursors or formation of higher molecular weight species, and then whitening occurs with additional aging.

However, considerably less work has been done on nighttime aging mechanisms, which will occur with the NO_3 radical. NO_3 is a ubiquitous, highly reactive oxidant, formed *via* reactions between NO_x and ozone (O_3). In particular, it can rapidly participate in addition reactions with electron-rich functional groups, such as aromatic rings and double bonds,[32] and it can also drive H-atom abstraction. Noting that NO_3 exists in a dynamic equilibrium with N_2O_5, its mixing ratios can range from many tens to hundreds of pptv in polluted environments, down to a few pptv in cleaner environments such as forests and marine environments.[32] Within near-field wildfire plumes, the formation rates of NO_3 can be high (up to 1 ppbv per hour), but the mixing ratios are generally quite low, well below the pptv level,[33] because of the high reactivity of NO_3 with gas phase constituents, such as phenolic molecules. NO_3 mixing ratios may be higher farther from the fires, as many of the reactive co-emitted species have already been depleted or diluted, reducing its loss pathways.

A study using a laboratory surrogate for tar balls has indicated that NO_3 oxidative transformations of BrC materials give rise to more absorption in the visible part of the spectrum, likely through the formation of $-NO_2$ groups (and perhaps $-O-NO_2$ groups) on aromatic rings,[34] with analogous chemistry of NO_3 observed in the aqueous phase[35] and with aqueous droplets.[36,37] NO_3 aging is consistent with some field observations of nighttime aging.[38] Potential mechanisms for this chemistry, as illustrated in Scheme 1, involve NO_3 addition to the ring or H-abstraction from the phenolic OH group, with subsequent NO_2 addition to the free radical site on the ring to regain aromaticity.[36,37,39–41] We note that NO_3 chemistry may form products similar to those that are formed from OH chemistry in a NO_x-rich environment when H-abstraction occurs, whereas O_3 oxidation more likely leads to ring-opening products.

Multiphase chemistry kinetic studies have largely focused on the interactions of gas-phase NO_3 with individual biomass burning materials, including phenolic substances such as catechol.[36,37] For example, by directly monitoring NO_3 decay, one study reports a reactive uptake coefficient of NO_3 with nitroguaiacol films on the order of 0.02 with no dependence on relative humidity up to 60%. A second study reports larger uptake coefficients, roughly 0.3, for reactions of NO_3 with syringaldehyde, vanillic acid, and coniferyl aldehyde using a relative rate technique and UV photoionization aerosol mass spectrometry;[39] both nitro- and di-nitro-products were observed. Such large uptake coefficients are consistent with the results of past studies showing that NO_3 reactivity with aromatic molecules in the form of polycyclic aromatic hydrocarbons is very efficient, with reactive uptake coefficients larger than 0.1.[42,43] Most recently, wood smoke particles have been shown to react on the timescale of minutes with part per trillion levels of NO_3, forming nitrated products that absorb across the UV and visible parts of the spectrum.[31]

To advance our understanding of the chemistry involving nighttime aging of BrC wood smoke particles, our goals in this work are to measure the reaction kinetics for the addition of $-NO_2$ groups to a typical wood smoke condensed-phase aromatic compound – vanillic acid – while simultaneously observing the ability of the particles to absorb light in the near UV and visible parts of the spectrum. We chose vanillic acid as the surrogate molecule to study, given its prevalence in wood smoke,[44,45] low volatility (2×10^{-8} atm),[46] which ensures that it is a particulate species, and aromaticity. We conducted the experiment in an aerosol flow tube with online instrumentation for monitoring changes in particle composition and optical properties. The experiments were performed with pptv-level, atmospherically relevant NO_3 mixing ratios.

2. Methods

2.1 Experimental

Experiments were conducted in a glass aerosol flow tube reactor (inner diameter 14.4 cm, length 200 cm, see Fig. 1) operated in a steady state manner at 296 ± 2 K and atmospheric pressure. As described below, variable reaction times within the reactor were achieved by the introduction of gas-phase NO_2 *via* a movable injector, whereas aerosol particles and O_3 were injected at the upstream end of the flow tube. The sealed glass reactor was wrapped in aluminum foil, oriented vertically, and operated with a total flow of zero air, 1.6 SLM, which corresponds to a maximum residence time of 15 minutes. The relative humidity in the flow tube was raised by removing the dryers after the atomizer. The RH was measured using a probe (model RH-USB,

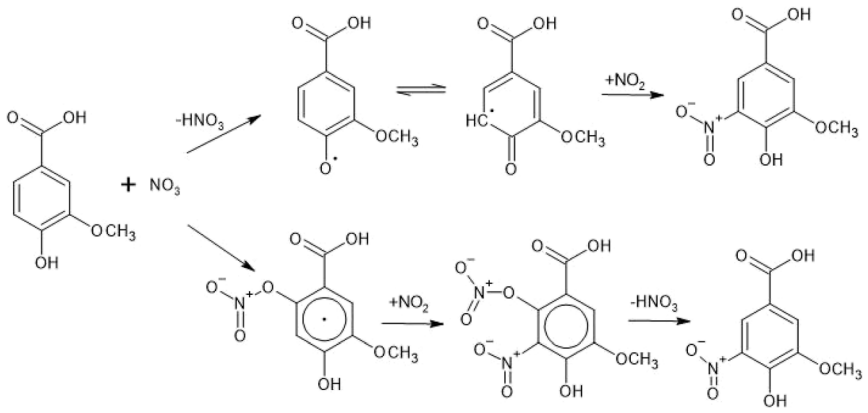

Scheme 1 Potential mechanisms for the reaction of NO_3 with vanillic acid.

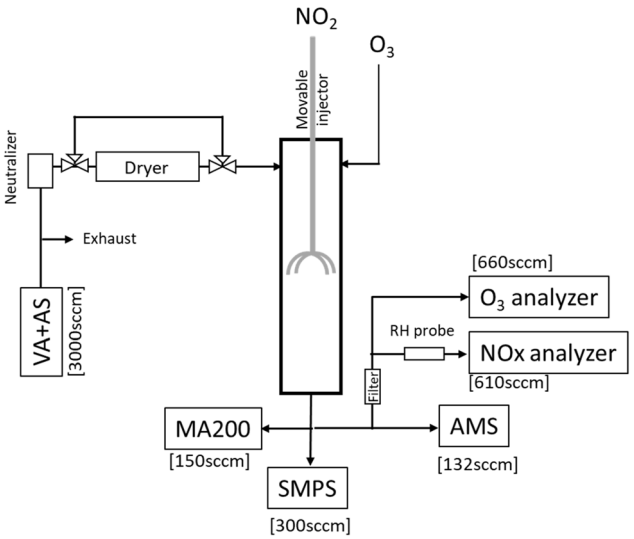

Fig. 1 Schematic of the experimental apparatus.

Omega Engineering Inc.) located on the flow exiting the reactor. It was steady to ±1.5% for an individual experiment.

Instrumentation attached to the flow tube included a scanning particle mobility sizing (SMPS) system (Model 3034, TSI) for aerosol particle size determination, with the sheath at the same RH as the sample flow. Connected to the flow tube *via* conductive polymer tubing and stainless steel, the SMPS was operated with a sample flow of 0.3 SLM and a sheath flow of 3 SLM, with a scan rate of 4 minutes. A high-resolution aerosol mass spectrometer (HR-AMS) provided aerosol particle composition information *via* flash vaporization of aerosol particles at 600 °C, followed by electron-impact ionization of volatilized molecules.[47] The AMS sampled aerosol particles at a flow rate of 132 sccm through conductive polymer tubing and metal tubing. It was operated in V-mode and was calibrated with ammonium nitrate particles such that the aerosol masses presented in the paper are in nitrate-equivalent mass. The default relative ionization efficiency (*i.e.*, relative to nitrate, RIE) of 1.2 was applied to determine sulfate mass loadings. Both vanillic acid and nitrovanillic acid (a potential reaction product, see Scheme 1) were calibrated directly using size-selected (300 nm), atomized particles. Their RIE values were 0.011 and 0.006, respectively.

To measure the ability of the particles to absorb light from the near ultraviolet to the near infrared parts of the spectrum, a 5-wavelength aethalometer (MA200, Aethlabs Inc., 375, 470, 528, 625, 880 nm) was used with measurements reported every minute. MA200 aethalometers operate by sampling aerosol particles onto a Teflon filter with a flow rate of 150 sccm, with the changes in light attenuation monitored continually. The standard correction provided by the supplier to account for the scattering effects on the filter ($C_{ref} = 1.3$) was applied to obtain the mass absorption cross section at each wavelength.[48] The dual spot correction was employed to compensate for the reduction in light attenuation caused by the material accumulating on the filter, following the method from Virkkula *et al.*[49,50]

Aerosol particles were injected through a side-arm injector at the upstream end of the flow tube. The particles had a polydisperse size distribution, formed *via* atomization of an aqueous solution of ammonium sulfate (0.005–0.007 M, AS) and vanillic acid (0.007–0.010 M). AS was used for three reasons: its environmental relevance, ability to add hygroscopicity to the particles, and utility as an unreactive aerosol component to act as an internal standard. The geometric mean diameter of the aerosol size distribution was approximately 95 nm and mass loadings in the reactor were approximately 500 μg m^{-3}.

NO_3 was generated *in situ* within the flow reactor by the reaction of gas-phase O_3 and nitrogen dioxide (NO_2). In particular, O_3 within a 250 sccm flow of zero air was added at the upstream end of the flow tube and NO_2 was supplied as a 10 sccm flow from a cylinder (3 ppm NO_2 in N_2) *via* a movable, stainless steel injector (6.5 mm o.d., 210 cm long) configured with four exit ports aligned with the flow direction. In particular, the NO_2 flowed through a 3 mm o.d. Teflon tube that lay inside the stainless-steel injector. The O_3 was generated by passing 1000 sccm of zero air over a Hg lamp housed in a glass cell. The mixing ratios of NO_2 and O_3 in the flow tube were 21 (±4) and 230 (±15) ppbv, respectively, as measured continuously *via* gas monitors (Thermo NOx analyzer model 42i and 2B Tech, Model 202 Ozone Monitor) connected to the exit flow.

Sliding through an o-ring seal, the injector could be moved vertically within the flow tube to provide variable reaction times between the NO_3 (that forms from the reaction of NO_2 and O_3) and aerosol particles within the main flow. The injector was electrically grounded to minimize the loss of particles on it.

In the kinetics determinations described below, we only used the data collected with a minimum residence time of roughly 2 minutes within the flow tube. There are two reasons for this. One, an estimate of the diffusive mixing time for the NO_2 exiting the injector within the carrier gas of the flow is a couple of minutes. Two, a kinetics model (see SI Text S1 and Fig. S2) predicts that NO_3 will achieve a quasi-steady state concentration in the flow tube on the timescale of less than 2 minutes.

The mixing ratio of NO_3 in the flow reactor was measured using an indirect tracer method during independent experiments in the flow tube, *i.e.*, these experiments were not conducted at the same time as the NO_3/VA/AS experiments. We added ozone and α-pinene (2 ppbv initial mixing ratio) to the flow tube. A proton-transfer-reaction mass spectrometer (PTR-MS) monitored the change in α-pinene signal, using the H_3O^+ reagent ion at m/z 137,[51] with and without NO_2 present, *i.e.*, with and without NO_3 present. The NO_3 concentration was calculated from the following equation:

$$[NO_3] = -\frac{\ln\left([\alpha\text{-pinene}]/[\alpha\text{-pinene}]_0\right)}{k_\alpha \times t} \quad (1)$$

where k_α is the rate constant of NO_3 with α-pinene, t is the time in the reactor and $[\alpha\text{-pinene}]_0$ and [α-pinene] are the concentrations of α-pinene before and after injection of NO_2 into the reactor. The α-pinene was added *via* a cylinder containing a dilute mixture (21 ppmv) of the gas in N_2. The particle loading and the O_3 and NO_2 mixing ratios were the same as during the VA kinetics experiments. Sufficiently little α-pinene was added that its reaction with NO_3 did not represent a major sink relative to the loss of NO_3 *via* reactions with NO_2, particles, and the walls of the reactor. Additional details on the measurements of the NO_3 concentrations are provided in the SI (Text S1, Fig. S1, S2 and Table S1).

Lastly, offline ultraviolet-visible spectra of stock solutions were measured with an Ocean Optics spectrometer (model USB 2000+) equipped with a deuterium tungsten halogen light source (DT-Mini-2, Ocean Optics). The light-absorption spectra were analyzed using the SpectraSuit (Ocean Optics) software with spectral data ranging between 250 and 850 nm. A water blank was measured prior to each measurement and subtracted from all spectra.

2.2 Data analysis

The reactive uptake coefficient expresses the probability that a reaction occurs upon collision of NO_3 with an aerosol particle. In this work, we define the reactive uptake coefficient as representing the probability that a condensed phase nitrated product forms from the reaction, as observed with the AMS. To do this, we use eqn (2) to calculate the uptake coefficient:[52]

$$\gamma_{NO_3} = \frac{-\mathrm{d}\left([VA]_t/[VA]_0\right)}{\mathrm{d}[NO_3]t} \times \frac{V}{A} \times \frac{4RT}{\nu} \times [\text{reactant}]_0 \quad (2)$$

where the differential term is the slope of the linear fit of the decay of the particle mass concentration of reactive vanillic acid in the flow tube, [VA], relative to the NO_3 exposure; V/A represents the particle volume to surface area ratio, ν is the mean speed of nitrate radicals in the gas phase, R is the gas constant and T is the temperature. The initial molar concentration of reactive vanillic acid in the particles, $[\text{reactant}]_0$, was estimated using the following:

$$[\text{Reactant}]_0 = \frac{\rho_{VA}}{MW_{VA}} \times \left(\frac{[NVA]}{[Org]}\right)_\infty \quad (3)$$

where ρ_{VA} represents the density of vanillic acid, MW_{VA} is the molecular weight of vanillic acid (168.13 g mol^{-1}), $[NVA]_\infty$ and $[Org]_\infty$ are the particle mass concentrations of nitrovanillic acid (NVA) and total organics in the flow tube, respectively, taken at infinite reaction time. Note that for this analysis, the AMS parent ion for NVA is used to indicate product formation. We extrapolate the kinetics data to infinite reaction time to provide an estimate of the maximum amount of product that can form. We note that higher-order products such as dinitrovanillic acid are also formed (see discussion below), it is likely that at least part of the mono-nitrovanillic ion signal in the AMS originates from the fragmentation of these compounds. We assume that the amount of reactive VA is equal to the total amount of NVA that forms, *i.e.*, some of the VA may be buried in the solid particle and cannot react. Although we are measuring reaction products (*i.e.*, NVA) with the AMS, eqn (2) requires knowledge of the amount of the reactive starting material ([VA]):[53]

$$[VA]_t = [VA]_0 - [NVA]_t = [NVA]_\infty - [NVA]_t \quad (4)$$

For large uptake coefficients, there can be a mass transfer limitation arising from the slow diffusion of NO_3 in the gas phase to the particle, which can be accounted for using a standard approach.[54] In particular, by calculating the Knudsen number characteristic for the system, one can correct an observed first-order rate constant for reactant loss for gas-phase diffusion. For the results presented below, the correction is less than 15%, which is within the estimated uncertainty in the uptake coefficient.

3. Results and discussion

3.1 Nitrate radical concentration

Fig. S1 illustrates typical data from which the concentration of NO_3 was determined. The average PTR-MS signal for α-pinene was calculated when NO_2 (and so, also, NO_3) was present in the flow tube and when it was absent. Considering the residence time of air in the flow tube (900 seconds for these experiments), eqn (1) was used to determine that the NO_3 concentration was 3.6 and 4.1 × 10^7 molecules per cm^3 at 25% ± 5% and 55 ± 5% RH, respectively, yielding an average value of 3.8 ± 1.9 × 10^7 molecules per cm^3 (*i.e.*, 1.6 ± 0.8 pptv at room temperature and pressure) across 7 experiments. See Text S1 for more details. The variability in RH values represents variations from experiment to experiment.

It is important to determine the timescale at which NO_3 goes into a quasi-steady state within the flow tube, after NO_2 and O_3 react. The chemical reactions occurring in the flow tube include the following:

$$NO_2 + O_3 \rightarrow NO_3 + O_2 \quad (R1)$$

$$NO_3 + NO_2 \rightarrow N_2O_5 \quad (R2)$$

$$N_2O_5 \rightarrow NO_3 + NO_2 \quad (R3)$$

$$NO_3 + \text{particle} \rightarrow \text{products} \quad (R4)$$

$$N_2O_5 + \text{particle} \rightarrow \text{products} \quad (R5)$$

When (R1)–(R5) are implemented into a numerical model, the NO_3 concentration temporal profile in Fig. S2 is generated. Most importantly, NO_3 moves into steady state within about 100 seconds. As stated above, this is one reason that we do not use kinetic data collected within the first 20 cm of the flow tube, corresponding to 2 minutes of residence time after the NO_2 and O_3 mix.

The predicted concentration of NO_3 is within a factor of 6 of the measured value, with the discrepancy likely due to neglecting NO_3 and N_2O_5 wall losses in the model. However, note that if reaction (R4) is not included in the model, the predicted NO_3 concentration is roughly 30 times larger than the measured value. This is indirect confirmation that NO_3 reacts rapidly with the aerosol particles.

3.2 Reaction kinetics between NO_3 and vanillic acid aerosol particles

Fig. 2 illustrates a typical time series of quantities monitored by the AMS during an experiment, as the injector was moved to change the NO_3 residence time in the flow tube. SO_4^{2-} decreased somewhat at longer reaction times (upper horizontal axis), likely due to small fluctuations in the flow conditions or atomizer output. Given that ammonium sulfate is present in the atomizer alongside vanillic acid, VA and AS will be internally mixed within the same particles. Thus, we use SO_4^{2-} as an internal standard to correct for changes in the AMS particle collection efficiency that can occur with changing particle composition. After SO_4^{2-} normalization, the VA signal (observed at its molecular ion, $C_8H_8O_4^+$) decreases with longer reaction times and the NVA signal ($C_8H_7NO_6^+$) increases, indicative of a multiphase reaction of VA with NO_3 to form NVA (and other products).

Fig. 2 demonstrates that significant nitration of the particles is occurring, as indicated by the increase in the total nitrate signal with increasing reaction time in the flow tube. AMS total nitrate can arise from either inorganic nitrate (*i.e.*, NO_3^-) or oxidized organic nitrogen (*e.g.*, R-NO_x) particulate matter, which have different NO^+/NO_2^+ ratios in the particle AMS mass spectra. In particular, in our instrument, NH_4NO_3 particles yield a NO^+/NO_2^+ ratio of 1.3, whereas higher values are typical of organic nitrate/nitro compounds.[55] Thus, the high ratios in Fig. 2 are indicative of oxidized organic nitrogen products. For reference, we note that we measured the NO^+/NO_2^+ ratio for nitrovanillic acid aerosol particles ($C_8H_7NO_6$) to be 12.5 in our instrument.

While we clearly observed NVA formation, there was some evidence for the addition of two –NO_2 groups to the VA aromatic ring (*i.e.*, $C_8H_7NO_6^+$ and $C_8H_6N_2O_8^+$). However, the di-nitro product signal was weaker than the mono-nitro signal (see Fig. S3), so only the mono-nitro product signal is plotted in Fig. 2. We note that the AMS employs electron impact as its ionization mechanism, which induces considerable ion fragmentation. Thus, the signal plotted in Fig. 2 for the mono-nitro product may also have some mass spectral intensity arising from fragmentation of larger parent ions. The ratio of the mono- to di-nitro signals did not vary during the course of the reaction. Note that the same two products were observed in the only prior study of this reaction, which used a softer ionization technique.[39]

The normalized signal of the product $C_8H_7NO_6^+$ in Fig. 2 is plotted in Fig. 3a *versus* residence time in the flow tube, clearly indicating that the product intensity grows with increasing reaction time. Note that there is curvature in the growth curve, with slower growth at long reaction times. We attribute the slowing of the reaction at long times to the depletion of VA available for reaction at the surface of the solid VA/AS particles. To support this claim, we can estimate the number of VA molecules available for reaction at the surface of the particles. In particular, this quantity is calculated to be approximately from 0.7 to 1.4 $\times$ 10^{10} molecules per cm^3, obtained by multiplying the particle surface area density in the flow tube (6.8 $\times$ 10^{-5} cm^2 cm^{-3}) by a typical monolayer molecule coverage for molecules the size of VA ($\approx$1 to 2 $\times$ 10^{14} molecules per cm^2). We can also estimate the number of reactive collisions per unit volume ($\approx$6 $\times$ 10^9 reactions per cm^3) that particles experience when passing through the flow tube by multiplying eqn (S1) by the steady state [NO_3] and the total reaction time (1000 s), assuming the reactive uptake coefficient is 0.3 (see below for calculation of the uptake coefficients). The fact that these two quantities are calculated to be so similar to each other says that there is enough NO_3 in the flow tube, and that it has sufficiently high reactivity, that it can react with every VA molecule present at the surfaces of the particles during the reaction time in the flow tube; this makes us believe that the reaction is only occurring at the surface of the particles.

In Fig. 3b, we plot the kinetics data in Fig. 3a *versus* NO_3 exposure, *i.e.*, the product of [NO_3] and reaction time. The *y*-axis of Fig. 3b is the quantity [VA] at time *t*, divided by the initial concentration of VA available for reaction, as calculated *via* eqn (4), where the value of $[VA]_0$ is determined by fitting the data in Fig. 3a with a non-linear, least squares, exponential growth curve.

According to eqn (2), the slope of the linear least squares fit to the data in Fig. 3b yields the reactive uptake coefficient for the formation of nitrated VA. For the data in this figure, the uptake coefficient is determined to be 0.10 $\pm$ 0.02, where this uncertainty arises from the precision of the straight line fit to the data. Additional uncertainties in the uptake coefficient are larger, arising largely from the estimate of the value of

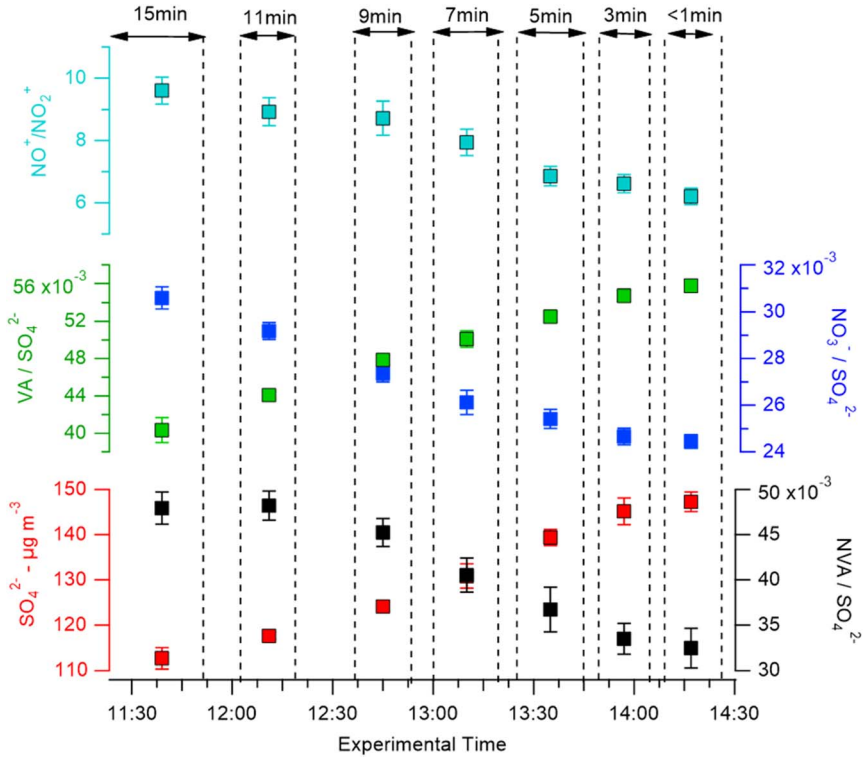

Fig. 2 Data collected during a typical experiment (RH = 25%), where experimental time on the lower horizontal axis is the real time at which the measurements were conducted in the laboratory, plotted in the hh:mm format. The times on the upper horizontal axis (*i.e.*, <1 to 15 min) correspond to the variable reaction times of NO_3 and particles in the flow tube, dependent on the injector position, where the first time bracket at 15 min represents the maximum exposure time, which decreases as the injector is pushed into the flow tube. Traces shown include aerosol sulfate (SO_4^{2-}), NO^+/NO_2^+, and SO_4^{2-}-normalized vanillic acid (VA), nitrate (indicative of both inorganic and organic nitrates), and NVA.

[reactant]$_0$ (±50%) and a systematic error in the concentration of NO_3 in the flow tube (±50%). A summary of all the uptake coefficient measurements is provided in Table 1. The errors listed in the table are one standard deviation precision errors. The relatively large precision errors are likely a result of a variety of factors, including relatively weak AMS signals arising from products only forming on the surface of the solid particles, as well as variability in the aerosol flow tube conditions.

The overall conclusion is that this multiphase reaction occurs rapidly, with reactive uptake coefficients larger than 0.1. This high reactivity is consistent with most past studies of related systems for the reactions of NO_3 with aromatic, electron-

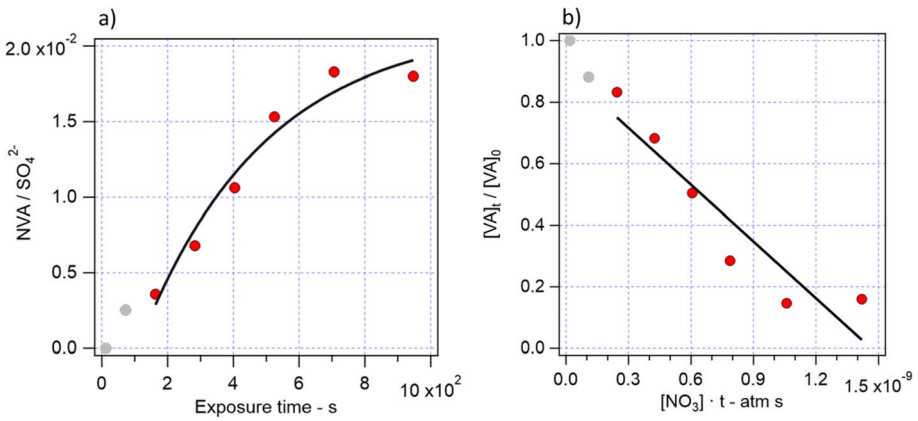

Fig. 3 (a) For the data in Fig. 2, the nitro-vanillic acid-to-sulfate ratio for different reaction exposure times in the flow reactor, and (b) variation in vanillic acid mass loading at each time normalized to the initial vanillic acid mass loading, as a function of NO_3 exposure in the flow tube. Note that the nitro-vanillic acid data are baseline corrected by the signal with zero reaction time. Only the red data points are used in the kinetics analysis, whereas the grey points at early times are not included in the fits (since the first 2 minutes are required for NO_3 to reach steady state).

Table 1 Uptake coefficients obtained from the experiments under low and high relative humidity conditions, where the uncertainty is the precision of individual experiments

RH	25% ± 5%	55% ± 5%	All
Number of experiments	4	4	8
Uptake coefficient	0.30	0.19	0.25
Uncertainties	0.39	0.12	0.27

rich species, as presented in the Introduction. In particular, the values are in excellent agreement with the only prior measurements in the literature for reaction with VA, where large values of the uptake coefficient (0.28) were also reported.[39] While we cannot say this with confidence based on the uncertainties, there is an indication that the reaction is slower at higher RH, which is consistent with the quantity of $(NVA/org)_\infty$ also being lower at high RH. This is in agreement with a report from the literature that the rate of the reaction of NO_3 with wood smoke particles is also slower at higher RH.[31] The reasons for this are unclear. Given that vanillic acid is solid for all conditions (*i.e.*, it has a low solubility of 1.5 g L^{-1} (ref. 46)), it is likely phase separated from AS. Perhaps, water competes with NO_3 for reactive sites. Alternatively, low RH may restrict reactants to the surface of the particles, making them more likely to react more than once with NO_3.

3.3 Changes in aerosol particle optical properties *via* NO_3 reaction

From an atmospheric perspective, it is important to determine how fast VA particles become more optically absorptive upon reaction with NO_3. To that end, simultaneous with the AMS measurements, we also measured the change in particulate absorption as a function of exposure time in the flow tube. For the data shown in Fig. 2–4 illustrates that the absorption at 375 nm increases steadily with increasing reaction time, with the rate of absorption increase accelerating at long reaction times. Equivalent data are shown for longer wavelengths in Fig. S4.

The increase in absorption presumably arises because nitration of an aromatic ring leads to enhanced electron delocalization. This is clearly illustrated by aqueous phase absorption spectra of solutions of NVA and VA (Fig. 5). In particular, NVA has a strong absorption feature in the near UV that extends beyond 300 nm to roughly 400 nm. Commercial standards of dinitro-vanillic acid are not available, but it is expected that polynitrated products will lead to more electron delocalization and longer wavelength absorption.

Also shown in Fig. 5 are absorption spectra as measured by the aethalometer, both with and without NO_3 exposure. The aerosol particle absorption spectra clearly show that enhanced absorption arises with NO_3 exposure not only in the near UV, where nitrovanillic acid is an efficient absorber, but also well into the visible part of the spectrum. This is indicative of a high degree of chemical processing that has occurred in the particles, giving rise to much more highly absorbing species. While

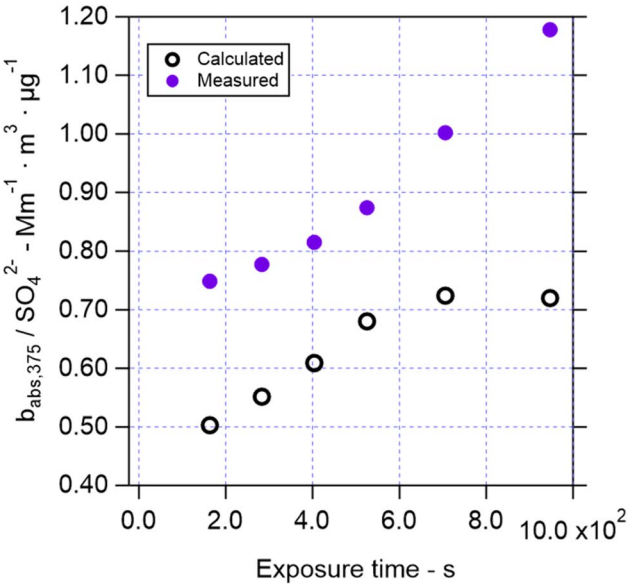

Fig. 4 Example of absorption coefficients (units of Mm^{-1}) at 375 nm, with normalization by sulfate AMS loading (units of $\mu g\ m^{-3}$) at RH = 25% ± 5%, for the data in Fig. 2 and 3. The measured values were obtained from the aethalometer. The predicted values arise from the measurements of mass loading of NVA in the flow tube and the measured MAC value for NVA.

consistent with the AMS observation of dinitro-vanillic acid product formation, a much wider range of products may also be forming. Absorption that extends into the visible part of the spectrum was also observed during the nitration of catechol with HONO, potentially through the formation of higher-order reaction products.[56]

Confirmation that nitrovanillic acid is not the sole product of the reaction comes from Fig. 4, where the predicted absorption arising from this product is plotted alongside the observed absorption change. In particular, using the NVA commercial

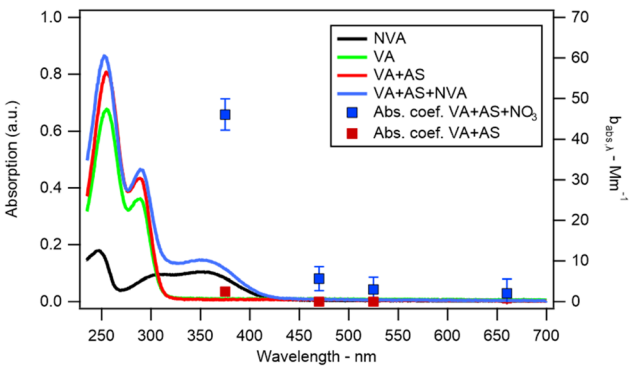

Fig. 5 Absorption spectra of aqueous solutions of vanillic acid (VA, green); vanillic acid and ammonium sulfate (VA + AS, red); nitrovanillic acid (NVA, black); vanillic acid, ammonium sulfate and nitrovanillic acid (VA + AS + NVA, light blue). Aethalometer absorption coefficient measurements from a typical experiment at low relative humidity, with (blue squares) and without (red squares) NO_3 exposure, are also included.

standard, we measured its mass absorption coefficient (MAC, $m^2\ g^{-1}$) by atomizing an aqueous solution of this compound and measuring its absorption with the aethalometer. The mass concentration of the atomized particles was determined by AMS. The measured values for the MAC were: 15.0 $m^2\ g^{-1}$ at 375 nm, 0.80 $m^2\ g^{-1}$ at 470 nm, 0.25 $m^2\ g^{-1}$ at 525 nm, 0.17 $m^2\ g^{-1}$ at 660 nm. Using this MAC value, together with the calibrated AMS NVA signal and its measured RIE value, we predicted the amount of absorption that should arise in the particles from this product alone. Fig. 4 illustrates that these predicted values at 375 nm are similar to, but lower than, the observed values, with the discrepancy being significantly larger at long reaction times, likely due to additional product formation, such as dinitro species. It would be useful in future experiments to conduct high-resolution LC-MS measurements of reaction products collected on a filter.

4. Environmental implications

The major environmental implications arising from this work relate to the demonstration of rapid brown carbon aging associated with the reaction between vanillic acid and nitrate radicals. In particular, the gas-particle chemistry is very fast, with a NO_3 uptake coefficient on the order of 0.25, leading to the formation of nitrophenolic products. Such fast kinetics are in excellent agreement with the only prior measurements of this uptake coefficient and with reactions involving other electron-rich substrates.[39] In addition, it is known that the gas-phase rate constants for the reaction between NO_3 and phenolic compounds are close to gas kinetics, with rate constants on the order of 10^{-10} cm^3 per molecule per s.[57]

Within a wildfire plume, the gas phase mixing ratios of many compounds, including phenols, are so high that modeled mixing ratios of NO_3 are much less than 1 pptv within a few hours of the fire.[33,58] These models predict that the multiphase loss of NO_3 does not represent a significant NO_x sink under such conditions because the gas phase chemistry proceeds so rapidly. It is unlikely that particulate brown carbon formation will proceed rapidly in this regime, where NO_3 mixing ratios are strongly suppressed.

However, downwind from the fire, gas phase mixing ratios of reactive VOCs will be significantly lower *via* dilution or reaction, so that the NO_3 sink will be smaller and NO_3 mixing ratios correspondingly higher. In addition, the production rate of NO_3 can be sustained at high levels, in part because O_3 formation can occur within wildfire plumes[59–61] and in some cases, decomposition of organic nitrates leads to NO_2 formation. Indeed, if wildfire plumes enter polluted regions, then NO_3 mixing ratios can be quite high, on the order of tens to hundreds of pptv.[32]

The rapid BrC-forming chemistry observed in this work occurred with an NO_3 exposure (equal to the NO_3 mixing ratio multiplied by time) of 3400 pptv s, *i.e.*, for a mixing ratio of 3.8 pptv over 15 minutes. Thus, if the NO_3 mixing ratios are suppressed by gas phase reactivity to 0.1 pptv, then the chemistry we observed in the flow tube would occur over roughly 10 hours, *e.g.*, during one night. However, if the NO_3 mixing ratios are elevated to 10 pptv, then the chemistry will occur on the timescale of only a few minutes.

While these experiments were conducted at room temperature, wildfire plume injection heights are frequently a few kilometers into the free troposphere, where the temperatures are lower. Given that we saw fast chemistry with solid vanillic acid surfaces at low RH, the chemistry described in this paper will likely still occur under such conditions when many organic particles become more viscous or semi-solid. The kinetics of this chemistry at much higher RH values than explored in this work, where vanillic acid may be more solubilized, will be important to explore in future work.

Although this paper emphasizes the connections of this chemistry to wildfire BrC, the same rapid formation of light-absorbing compounds will occur with phenolic substances present in urban environments. Phenols form readily from the photooxidation of aromatic precursors, such as the formation of phenol from benzene *via* oxidation by OH.[3] Given the recent identification of urban BrC[10,62,63] and known high levels of NO_3 in polluted regions,[32] it is possible that reactions of the type studied in this work may contribute to the formation of light-absorbing compounds in such settings.

Conflicts of interest

There are no conflicts to declare.

Data availability

The data are publicly available *via* the University of Toronto library at **https://doi.org/10.5683/SP3/JFR3LR** or **https://borealisdata.ca/dataset.xhtml?persistentId=doi:10.5683/SP3/JFR3LR**.

The supplementary information includes [1] a description of the estimation of NO_3 concentrations and kinetic model input parameters, [2] AMS signals of nitro-vanillic acid (NVA) compared with di-nitro VA, and [3] the effect of product formation on absorption coefficients at 375, 470, 528, and 625 nm. See DOI: **https://doi.org/10.1039/d5ea00066a**.

Acknowledgements

The Government of Canada's Environmental Damages Fund provided funding for this project under its Climate Action and Awareness Fund. The data are publicly available *via* the University of Toronto library at **https://doi.org/10.5683/SP3/JFR3LR**.

References

1 L. J. Kuo, P. Louchouarn and B. E. Herbert, Influence of combustion conditions on yields of solvent-extractable anhydrosugars and lignin phenols in chars: Implications for characterizations of biomass combustion residues, *Chemosphere*, 2011, **85**(5), 797–805.
2 K. M. Shakya, P. Louchouarn and R. J. Griffin, Lignin-Derived Phenols in Houston Aerosols: Implications for Natural

Background Sources, *Environ. Sci. Technol.*, 2011, **45**(19), 8268–8275.
3 R. Volkamer, B. Klotz, I. Barnes, T. Imamura, K. Wirtz, N. Washida, *et al.*, OH-initiated oxidation of benzene, *Phys. Chem. Chem. Phys.*, 2002, **4**(9), 1598–1610.
4 C. Liu, X. Zhang, Q. Wang and K. Shi, Role of PM2.5 in the photodegradation of the atmospheric benzene, *Environ. Pollut.*, 2019, **247**, 447–456.
5 M. O. Andreae and A. Gelencsér, Black carbon or brown carbon? The nature of light-absorbing carbonaceous aerosols, *Atmos. Chem. Phys.*, 2006, **6**(10), 3131–3148.
6 A. Laskin, J. Laskin and S. A. Nizkorodov, Chemistry of Atmospheric Brown Carbon, *Chem. Rev.*, 2015, **115**(10), 4335–4382.
7 L. Zeng, A. Zhang, Y. Wang, N. L. Wagner, J. M. Katich, J. P. Schwarz, *et al.*, Global Measurements of Brown Carbon and Estimated Direct Radiative Effects, *Geophys. Res. Lett.*, 2020, **47**(13), e2020GL088747.
8 A. Zhang, Y. Wang, Y. Zhang, R. J. Weber, Y. Song, Z. Ke, *et al.*, Modeling the global radiative effect of brown carbon: a potentially larger heating source in the tropical free troposphere than black carbon, *Atmos. Chem. Phys.*, 2020, **20**(4), 1901–1920.
9 T. S. Carter, C. L. Heald, C. D. Cappa, J. H. Kroll, T. L. Campos, H. Coe, *et al.*, Investigating Carbonaceous Aerosol and Its Absorption Properties From Fires in the Western United States (WE-CAN) and Southern Africa (ORACLES and CLARIFY), *J. Geophys. Res.: Atmos.*, 2021, **126**(15), e2021JD034984.
10 N. Y. Kasthuriarachchi, L. H. Rivellini, M. G. Adam and A. K. Y. Lee, Light Absorbing Properties of Primary and Secondary Brown Carbon in a Tropical Urban Environment, *Environ. Sci. Technol.*, 2020, **54**(17), 10808–10819.
11 A. Retama, M. Ramos-Cerón, O. Rivera-Hernández, G. Allen and E. Velasco, Aerosol optical properties and brown carbon in Mexico City, *Environ. Sci.: Atmos.*, 2022, **2**(3), 315–334.
12 A. Velazquez-Garcia, J. F. de Brito, S. Crumeyrolle, I. Chiapello and V. Riffault, Assessment of light-absorbing carbonaceous aerosol origins and properties at the ATOLL site in northern France, *Aerosol Res.*, 2024, **2**(1), 107–122.
13 H. Forrister, J. Liu, E. Scheuer, J. Dibb, L. Ziemba, K. L. Thornhill, *et al.*, Evolution of Brown Carbon in Wildfire Plumes, *Geophys. Res. Lett.*, 2015, **42**(11), 4623–4630.
14 X. Wang, C. L. Heald, A. J. Sedlacek, S. S. de Sá, S. T. Martin, M. L. Alexander, *et al.*, Deriving brown carbon from multiwavelength absorption measurements: method and application to AERONET and Aethalometer observations, *Atmos. Chem. Phys.*, 2016, **16**(19), 12733–12752.
15 X. Wang, C. L. Heald, J. Liu, R. J. Weber, P. Campuzano-Jost, J. L. Jimenez, *et al.*, Exploring the observational constraints on the simulation of brown carbon, *Atmos. Chem. Phys.*, 2018, **18**(2), 635–653.
16 Y. Zhang, H. Forrister, J. Liu, J. Dibb, B. Anderson, J. P. Schwarz, *et al.*, Top-of-atmosphere radiative forcing affected by brown carbon in the upper troposphere, *Nat. Geosci.*, 2017, **10**(7), 486–489.
17 R. A. Washenfelder, L. Azzarello, K. Ball, S. S. Brown, Z. C. J. Decker, A. Franchin, *et al.*, Complexity in the Evolution, Composition, and Spectroscopy of Brown Carbon in Aircraft Measurements of Wildfire Plumes, *Geophys. Res. Lett.*, 2022, **49**(9), e2022GL098951.
18 R. F. Hems, E. G. Schnitzler, C. Liu-Kang, C. D. Cappa and J. P. D. Abbatt, Aging of Atmospheric Brown Carbon Aerosol, *ACS Earth Space Chem.*, 2021, **5**(4), 722–748.
19 B. B. Palm, Q. Peng, C. D. Fredrickson, B. H. Lee, L. A. Garofalo, M. A. Pothier, *et al.*, Quantification of organic aerosol and brown carbon evolution in fresh wildfire plumes, *Proc. Natl. Acad. Sci.*, 2020, **117**(47), 29469–29477.
20 M. Zhong and M. Jang, Dynamic light absorption of biomass-burning organic carbon photochemically aged under natural sunlight, *Atmos. Chem. Phys.*, 2014, **14**(3), 1517–1525.
21 B. J. Sumlin, A. Pandey, M. J. Walker, R. S. Pattison, B. J. Williams and R. K. Chakrabarty, Atmospheric Photooxidation Diminishes Light Absorption by Primary Brown Carbon Aerosol from Biomass Burning, *Environ. Sci. Technol. Lett.*, 2017, **4**(12), 540–545; B. J. Sumlin, A. Pandey, M. J. Walker, R. S. Pattison, B. J. Williams and R. K. Chakrabarty, Correction to Atmospheric Photooxidation Diminishes Light Absorption by Primary Brown Carbon Aerosol from Biomass Burning, *Environ. Sci. Technol. Lett.*, 2018, **5**(3), 193.
22 E. G. Schnitzler and J. P. D. Abbatt, Heterogeneous OH oxidation of secondary brown carbon aerosol, *Atmos. Chem. Phys.*, 2018, **18**(19), 14539–14553.
23 J. P. S. Wong, A. Nenes and R. J. Weber, Changes in Light Absorptivity of Molecular Weight Separated Brown Carbon Due to Photolytic Aging, *Environ. Sci. Technol.*, 2017, **51**(15), 8414–8421.
24 C. Li, Q. He, J. Schade, J. Passig, R. Zimmermann, D. Meidan, *et al.*, Dynamic changes in optical and chemical properties of tar ball aerosols by atmospheric photochemical aging, *Atmos. Chem. Phys.*, 2019, **19**(1), 139–163.
25 J. P. S. Wong, M. Tsagkaraki, I. Tsiodra, N. Mihalopoulos, K. Violaki, M. Kanakidou, *et al.*, Atmospheric evolution of molecular-weight-separated brown carbon from biomass burning, *Atmos. Chem. Phys.*, 2019, **19**(11), 7319–7334.
26 L. T. Fleming, P. Lin, J. M. Roberts, V. Selimovic, R. Yokelson, J. Laskin, *et al.*, Molecular composition and photochemical lifetimes of brown carbon chromophores in biomass burning organic aerosol, *Atmos. Chem. Phys.*, 2020, **20**(2), 1105–1129.
27 C. Li, Q. He, Z. Fang, S. S. Brown, A. Laskin, S. R. Cohen, *et al.*, Laboratory Insights into the Diel Cycle of Optical and Chemical Transformations of Biomass Burning Brown Carbon Aerosols, *Environ. Sci. Technol.*, 2020, **54**(19), 11827–11837.
28 E. G. Schnitzler, T. Liu, R. F. Hems and J. P. D. Abbatt, Emerging investigator series: heterogeneous OH oxidation of primary brown carbon aerosol: effects of relative

humidity and volatility, *Environ. Sci.: Processes Impacts*, 2020, **22**(11), 2162–2171.
29 C. Liu-Kang, P. J. Gallimore, T. Liu and J. P. D. Abbatt, Photoreaction of biomass burning brown carbon aerosol particles, *Environ. Sci.: Atmos.*, 2022, **2**(2), 270–278.
30 C. Liu-Kang, A. Sokolova, Y. Gong, W. D. Fahy, H. Peng and J. P. D. Abbatt, Light Exposure of Wood Smoke Aerosol: Connecting Optical Properties, Oxidation, Radical Formation, and Chemical Composition, *ACS EST Air*, 2024, **1**(4), 273–282.
31 C. Liu-Kang, L. H. Rivellini, X. Wang and J. P. D. Abbatt, Rapid Nighttime Darkening of Biomass Burning Brown Carbon by Nitrate Radicals Is Suppressed by Prior Daytime Photochemical Aging, *ACS Earth Space Chem.*, 2025, **9**(5), 1124–1133.
32 S. S. Brown and J. Stutz, Nighttime radical observations and chemistry, *Chem. Soc. Rev.*, 2012, **41**(19), 6405–6447.
33 Z. C. J. Decker, M. A. Robinson, K. C. Barsanti, I. Bourgeois, M. M. Coggon, J. P. DiGangi, *et al.*, Nighttime and daytime dark oxidation chemistry in wildfire plumes: an observation and model analysis of FIREX-AQ aircraft data, *Atmos. Chem. Phys.*, 2021, **21**(21), 16293–16317.
34 C. Li, Q. He, A. P. S. Hettiyadura, U. Käfer, G. Shmul, D. Meidan, *et al.*, Formation of Secondary Brown Carbon in Biomass Burning Aerosol Proxies through NO3 Radical Reactions, *Environ. Sci. Technol.*, 2020, **54**(3), 1395–1405.
35 Y. Lei, X. Lei, G. Tian, J. Yang, D. Huang, X. Yang, *et al.*, Optical Variation and Molecular Transformation of Brown Carbon During Oxidation by NO3· in the Aqueous Phase, *Environ. Sci. Technol.*, 2024, **58**(7), 3353–3362.
36 M. S. Rana and M. I. Guzman, Oxidation of Catechols at the Air–Water Interface by Nitrate Radicals, *Environ. Sci. Technol.*, 2022, **56**(22), 15437–15448.
37 M. S. Rana, S. T. Bradley and M. I. Guzman, Conversion of Catechol to 4-Nitrocatechol in Aqueous Microdroplets Exposed to O3 and NO2, *ACS EST Air*, 2023, **1**(2), 80–91.
38 J. K. Kodros, D. K. Papanastasiou, M. Paglione, M. Masiol, S. Squizzato, K. Florou, *et al.*, Rapid dark aging of biomass burning as an overlooked source of oxidized organic aerosol, *Proc. Natl. Acad. Sci.*, 2020, **117**(52), 33028–33033.
39 C. Liu, P. Zhang, Y. Wang, B. Yang and J. Shu, Heterogeneous Reactions of Particulate Methoxyphenols with NO3 Radicals: Kinetics, Products, and Mechanisms, *Environ. Sci. Technol.*, 2012, **46**(24), 13262–13269.
40 B. Wei, J. Sun, Q. Mei, Z. An, X. Wang and M. He, Theoretical study on gas-phase reactions of nitrate radicals with methoxyphenols: Mechanism, kinetic and toxicity assessment, *Environ. Pollut.*, 2018, **243**, 1772–1780.
41 Z. Finewax, J. A. de Gouw and P. J. Ziemann, Identification and Quantification of 4-Nitrocatechol Formed from OH and NO3 Radical-Initiated Reactions of Catechol in Air in the Presence of NOx: Implications for Secondary Organic Aerosol Formation from Biomass Burning, *Environ. Sci. Technol.*, 2018, **52**(4), 1981–1989.
42 J. Mak, S. Gross and A. K. Bertram, Uptake of NO_3 on soot and pyrene surfaces, *Geophys. Res. Lett.*, 2007, **34**(10), L10804.
43 C. Liu, P. Zhang, B. Yang, Y. Wang and J. Shu, Kinetic Studies of Heterogeneous Reactions of Polycyclic Aromatic Hydrocarbon Aerosols with NO3 Radicals, *Environ. Sci. Technol.*, 2012, **46**(14), 7575–7580.
44 C. G. Nolte, J. J. Schauer, G. R. Cass and B. R. T. Simoneit, Highly Polar Organic Compounds Present in Wood Smoke and in the Ambient Atmosphere, *Environ. Sci. Technol.*, 2001, **35**(10), 1912–1919.
45 X. Wan, K. Kawamura, K. Ram, S. Kang, M. Loewen, S. Gao, *et al.*, Aromatic acids as biomass-burning tracers in atmospheric aerosols and ice cores: A review, *Environ. Pollut.*, 2019, **247**, 216–228.
46 PubChem. Vanillic Acid [Internet]. [cited 2025 Jul 6]. Available from: **https://pubchem.ncbi.nlm.nih.gov/compound/8468**.
47 F. Drewnick, S. S. Hings, P. DeCarlo, J. T. Jayne, M. Gonin, K. Fuhrer, *et al.*, A New Time-of-Flight Aerosol Mass Spectrometer (TOF-AMS) Instrument Description and First Field Deployment, *Aerosol Sci. Technol.*, 2005, **39**(7), 637–658.
48 M. Chakraborty, A. Giang and N. Zimmerman, Performance evaluation of portable dual-spot micro-aethalometers for source identification of black carbon aerosols: application to wildfire smoke and traffic emissions in the Pacific Northwest, *Atmos. Meas. Tech.*, 2023, **16**(9), 2333–2352.
49 A. Virkkula, T. Mäkelä, R. Hillamo, T. Yli-Tuomi, A. Hirsikko, K. Hämeri and I. K. Koponen, A simple procedure for correcting loading effects of aethalometer data, *J. Air Waste Manag. Assoc.*, 2007, **57**, 1214–1222.
50 A. Virkkula, X. Chi, A. Ding, Y. Shen, W. Nie, X. Qi, *et al.*, On the interpretation of the loading correction of the aethalometer, *Atmos. Meas. Tech.*, 2015, **8**(10), 4415–4427.
51 J. Krechmer, F. Lopez-Hilfiker, A. Koss, M. Hutterli, C. Stoermer, B. Deming, *et al.*, Evaluation of a New Reagent-Ion Source and Focusing Ion–Molecule Reactor for Use in Proton-Transfer-Reaction Mass Spectrometry, *Anal. Chem.*, 2018, **90**(20), 12011–12018.
52 I. J. George, A. Vlasenko, J. G. Slowik, K. Broekhuizen and J. P. D. Abbatt, Heterogeneous oxidation of saturated organic aerosols by hydroxyl radicals: uptake kinetics, condensed-phase products, and particle size change, *Atmos. Chem. Phys.*, 2007, **7**(16), 4187–4201.
53 S. D. Jorga, Y. Wang and J. P. D. Abbatt, Reaction of HOCl with Wood Smoke Aerosol: Impacts on Indoor Air Quality and Outdoor Reactive Chlorine, *Environ. Sci. Technol.*, 2023, **57**(3), 1292–1299.
54 N. A. Fuchs and A. G. Sutugin, *Highly Dispersed Aerosols*, Ann Arbor Science Publishers, 1970, p. 105.
55 D. K. Farmer, A. Matsunaga, K. S. Docherty, J. D. Surratt, J. H. Seinfeld, P. J. Ziemann, *et al.*, Response of an aerosol mass spectrometer to organonitrates and organosulfates and implications for atmospheric chemistry, *Proc. Natl. Acad. Sci.*, 2010, **107**(15), 6670–6675.
56 Y. Wang, S. Jorga and J. Abbatt, Nitration of Phenols by Reaction with Aqueous Nitrite: A Pathway for the Formation of Atmospheric Brown Carbon, *ACS Earth Space Chem.*, 2023, **7**(3), 632–641.

57 R. I. Olariu, I. Bejan, I. Barnes, B. Klotz, K. H. Becker and K. Wirtz, Rate coefficients for the gas-phase reaction of NO3 radicals with selected dihydroxybenzenes, *Int. J. Chem. Kinet.*, 2004, **36**(11), 577–583.
58 Z. C. J. Decker, K. J. Zarzana, M. Coggon, K. E. Min, I. Pollack, T. B. Ryerson, *et al.*, Nighttime Chemical Transformation in Biomass Burning Plumes: A Box Model Analysis Initialized with Aircraft Observations, *Environ. Sci. Technol.*, 2019, **53**(5), 2529–2538.
59 D. Jaffe, D. Chand, W. Hafner, A. Westerling and D. Spracklen, Influence of Fires on O3 Concentrations in the Western U.S, *Environ. Sci. Technol.*, 2008, **42**(16), 5885–5891.
60 D. A. Jaffe and N. L. Wigder, Ozone production from wildfires: A critical review, *Atmos. Environ.*, 2012, **51**, 1–10.
61 L. Xu, J. D. Crounse, K. T. Vasquez, H. Allen, P. O. Wennberg, I. Bourgeois, *et al.*, Ozone chemistry in western U.S. wildfire plumes, *Sci. Adv.*, 2021, **7**(50), eabl3648.
62 J. J. Devi, M. H. Bergin, M. Mckenzie, J. J. Schauer and R. J. Weber, Contribution of particulate brown carbon to light absorption in the rural and urban Southeast US, *Atmos. Environ.*, 2016, **136**, 95–104.
63 F. Costabile, S. Gilardoni, F. Barnaba, A. Di Ianni, L. Di Liberto, D. Dionisi, *et al.*, Characteristics of brown carbon in the urban Po Valley atmosphere, *Atmos. Chem. Phys.*, 2017, **17**(1), 313–326.